MULTIPLE IMAGING OF PSR B1133+16 BY THE INTERSTELLAR MEDIUM

YASHWANT GUPTA, N. D. RAMESH BHAT, AND A. PRAMESH RAO

National Centre for Radio Astrophysics, Tata Institute of Fundamental Research, Post Bag 3, Ganeshkhind, Pune-411 007, India

ABSTRACT

Refraction of pulsar radiation by electron density irregularities in the interstellar medium sometimes produces multiple imaging of pulsars, which can lead to periodic oscillations of intensity in pulsar dynamic spectra records. Such events can be used as tools to resolve the emission regions in pulsar magnetospheres. Here we describe results from the recent observation of a double imaging event for PSR B1133+16, which place fairly tight constraints on the location of the emission regions. Our analysis constrains the location of the scattering object to the shell of the Local Bubble. The phase of the oscillations shows significant variations across the pulse. The minimum value for the transverse separation of the emitting regions at the two edges of the pulse is inferred to be 3×10^5 m. This translates to a minimum emission altitude of 2.6×10^6 m. The nonmonotonic variations of the fringe phase with pulse longitude are interpreted as variations of the altitude of the emission regions for the orthogonal polarization modes of this pulsar. This is in agreement with theories where propagation effects, such as refraction, are responsible for the orthogonal modes.

Subject headings: ISM: general — ISM: structure — pulsars: individual (PSR B1133+16) — scattering

1. INTRODUCTION

Random electron density fluctuations in the ionized component of the interstellar medium (ISM) produce interstellar scintillation (ISS) of the radio signals received from pulsars. The small-scale irregularities ($\sim 10^7$ m) in the ISM produce a scatter-broadened image of the pulsar, characterized by the diffractive scattering angle, θ_d. The large-scale irregularities ($\sim 10^{11}$ m) steer the diffractive scattering cone by a mean direction of arrival, θ_r, which is expected to vary on refractive scintillation timescales. In dynamic spectra observations of pulsars, diffractive scintillation shows up as the random modulation of intensity across the time-frequency plane. The sloping nature of these intensity features at a single epoch is due to the refractive steering (see Rickett 1990 for a review of diffractive and refractive scintillations).

Sometimes, strong refraction effects in the ISM produce two or more scatter-broadened images of the pulsar with well-separated directions of arrival, θ_{r1} and θ_{r2}. Such multiple-imaging events produce additional features in pulsar dynamic spectra, such as multiple drift slopes and periodic intensity modulations or fringes, over and above the random modulations due to diffractive scintillation (e.g., Cordes & Wolszczan 1986; Gupta, Rickett, & Lyne 1994). Study of multiple imaging events allows a better understanding of the distribution of electron density irregularities in the ISM, particularly at large scales (e.g., Rickett 1996). An example of the application of this technique is the inference of enhanced scattering from a cloud of warm ionized medium from the analysis of a multiple imaging event detected for PSR B0834+06 (Rickett, Lyne, & Gupta 1997).

Multiple imaging events also provide an exciting technique for studying pulsar emission geometry, as they allow the possibility of resolving the pulsar magnetosphere. This happens because the phase of the fringes is sensitive to the transverse location of the source of radiation. Observed variations of this phase as a function of pulsar longitude can be used to infer the transverse separation of the emitting regions across the polar cap. This method was first used by Wolszczan & Cordes (1987) to resolve the emission region for PSR B1237+25, later on by Wolszczan, Bartlett, &

Cordes (1988) for PSR B1133+16, and more recently by Kuz'min (1992) for PSR B1919+21. From measurements of the phase change of the fringes from the leading to the trailing edge of the pulse, these authors report values ranging from 5×10^6 to 3×10^7 m for the transverse separation of the emission regions in the magnetosphere. For a dipole field geometry with constant emission altitude across the polar cap, these values translate to emission altitudes that are of the order of the light-cylinder distance (10^7–10^8 m). These estimates of emission altitudes are typically 1–2 orders of magnitude more than those estimated from other techniques such as period–pulse-width relationships, multifrequency timing (see Cordes 1992 for a summary), which infer emission altitudes in the range 10^5–10^6 m. In order to obtain an improved understanding of the location of emission regions in pulsar magnetospheres, it is important to resolve these differences. More accurate scintillation measurements that place tighter constraints on the size and location of emission regions can be very useful in this context.

In this paper we present the results from new observations of multiple imaging of the pulsar PSR B1133+16. The observations and analysis of the data are described in § 2. In § 3 we describe the model used to explain the multiple imaging episode and infer the size of the emission region for the pulsar from this. Section 4 discusses the implications of our results for the distribution of emission regions in pulsar magnetospheres. Our conclusions are summarized in § 5.

2. OBSERVATIONS AND DATA ANALYSIS

As part of a regular program for monitoring slow variations of diffractive scintillation properties of pulsars due to refractive scintillation, PSR B1133+16 was observed at 27 epochs from 1994 March to May, using the Ooty Radio Telescope (Bhat, Rao, & Gupta 1999b). The observations were carried out at a frequency of 327 MHz with a 9 MHz bandwidth spanned by 64 spectral channels. The dynamic spectra were generated by on-line averaging of 10 successive pulses, leading to an effective time resolution ≈ 12 s. The

data were gated around the on-pulse phase of the pulsar signal with a sampling interval of 6 ms, thereby providing 10 phase-resolved dynamic spectra with a resolution of 1°.8 of longitude. The details of the data analysis procedure are described in Bhat et al. (1999b).

Dynamic spectra at three epochs—1994 April 28 and 30 and May 2—in the observing session are shown in Figure 1. The dynamic spectra shown here are the sum from all the 10 longitude bins. There are a maximum of 512 time samples in these plots, and of the 64 frequency channels the display is restricted to channels 8–58. The intensity is represented on a linear gray scale with darker regions corresponding to higher intensity. The mean pulsar flux density for each epoch is indicated in the panels. The signal-to-noise ratio for these data is very good. For example, the mean signal-to-noise ratio for a data point in the dynamic spectrum for 1994 April 30 is estimated to be ≈ 23. The signal-to-noise ratio for the bright intensity scintles will clearly be 3–4

times more than this. When the data of the dynamic spectra are split into individual longitude bins, this signal-to-noise ratio is reduced, to first order, by a factor of $\sqrt{10}$, giving a mean signal-to-noise ratio for single-bin data of 7.3.

The broadband vertical white stripes in Figure 1 are due to residual intrinsic pulse-to-pulse intensity modulations of the pulsar that are not smoothed out in the 10 period averages. The random intensity fluctuations produced by diffractive ISS are clearly seen at all three epochs. Though located randomly, these intensity modulations (commonly referred to as scintles) have fairly well defined slopes in the frequency-time plane, which is due to the effect of large-scale, refractive phase gradients produced by the scattering medium (e.g., Hewish 1980). At all three epochs, the predominant slope is positive (i.e., scintles are aligned along increasing frequency and time). However, there is an indication, in the first two epochs, of the presence of some scintles with an opposite slope. Although single drift slopes are the
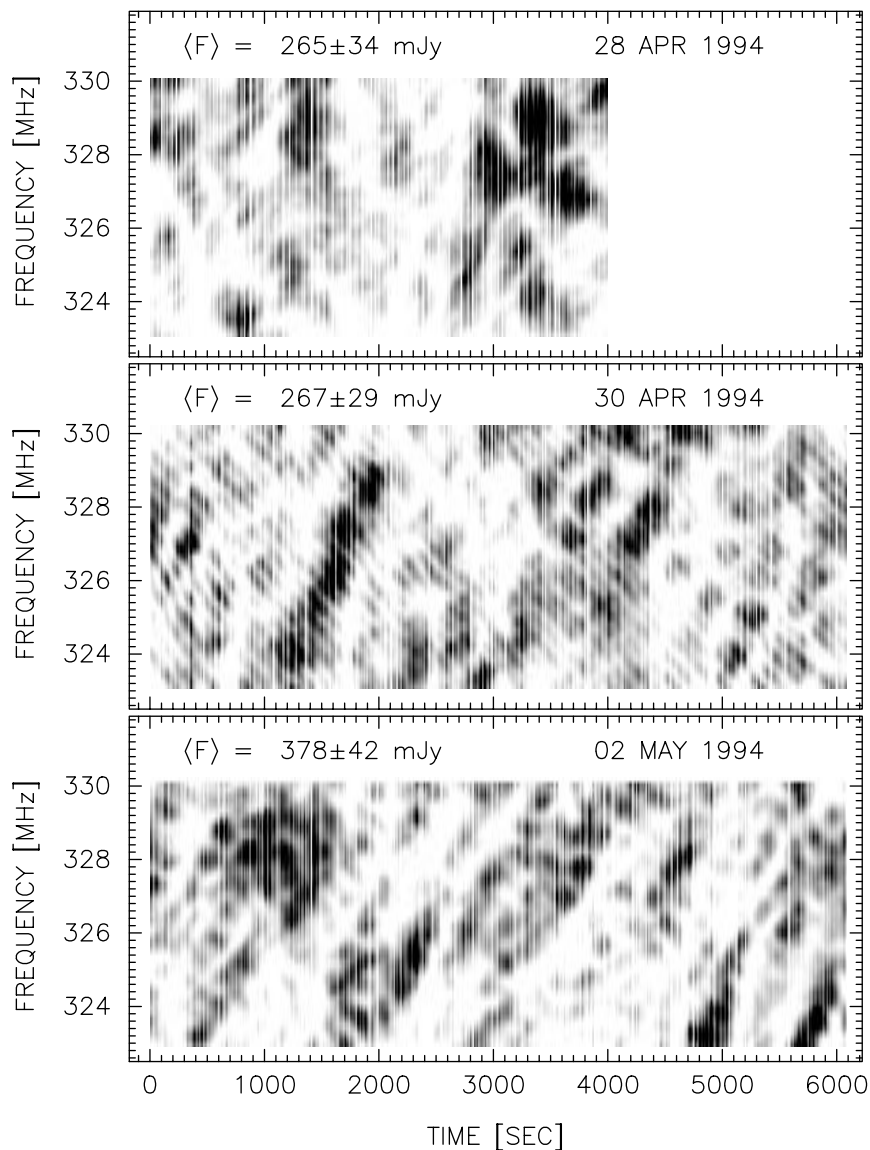

FIG. 1.—Dynamic scintillation spectra of PSR B1133+16 at 3 epochs. The intensity variations are represented in a linear gray scale, with darker regions corresponding to higher intensity values. The date of the observation is given at the top right of each panel, and the mean flux density at the top left of each panel.

norm, such occurrences of dual slopes in pulsar dynamic spectra are not uncommon (e.g., Hewish 1980). They are typical in cases where there are two well-separated directions of arrival for the refracted wave fronts.

A closer examination of the data from the second epoch (1994 April 30) reveals that in addition to the random intensity fluctuations due to diffractive ISS, periodic intensity modulations that are finer than the typical widths of the scintles are also present. Such periodic intensity modulations, commonly referred to as fringes, are typical indicators of the multiple imaging phenomenon. The data from the first and third epochs show no sign of such fringes, indicating that the phenomenon lasted for a fairly short time.

A secondary spectral analysis of the dynamic spectra data was carried out by performing a 512×64 point two-dimensional Fourier transform. The data were zero-padded to take care of the frequency channels rejected at the edges of the band. A periodicity in the primary dynamic spectra

should show up as a significant peak in the secondary spectra. For the data from the second epoch, a clear peak was found corresponding to a periodicity of

$$v_t = 5.9 \times 10^{-3} \text{ cycles s}^{-1},$$

$$v_f = 1.6 \text{ cycles MHz}^{-1} \tag{1}$$

in the inverse time and inverse frequency domains, respectively. However, the peak was not confined to a single bin in the secondary spectrum but was spread over about 5 bins along the inverse time axis and 4 bins along the inverse frequency axis.

To further elucidate the nature of the periodicities in the dynamic spectra, the data were put through a bandpass filter centered around the frequency of the periodic signal. The results are shown in the top panel of Figure 2, where the detailed nature of the periodicities is clearly brought out. The amplitude of the fringes is modulated by the ampli-
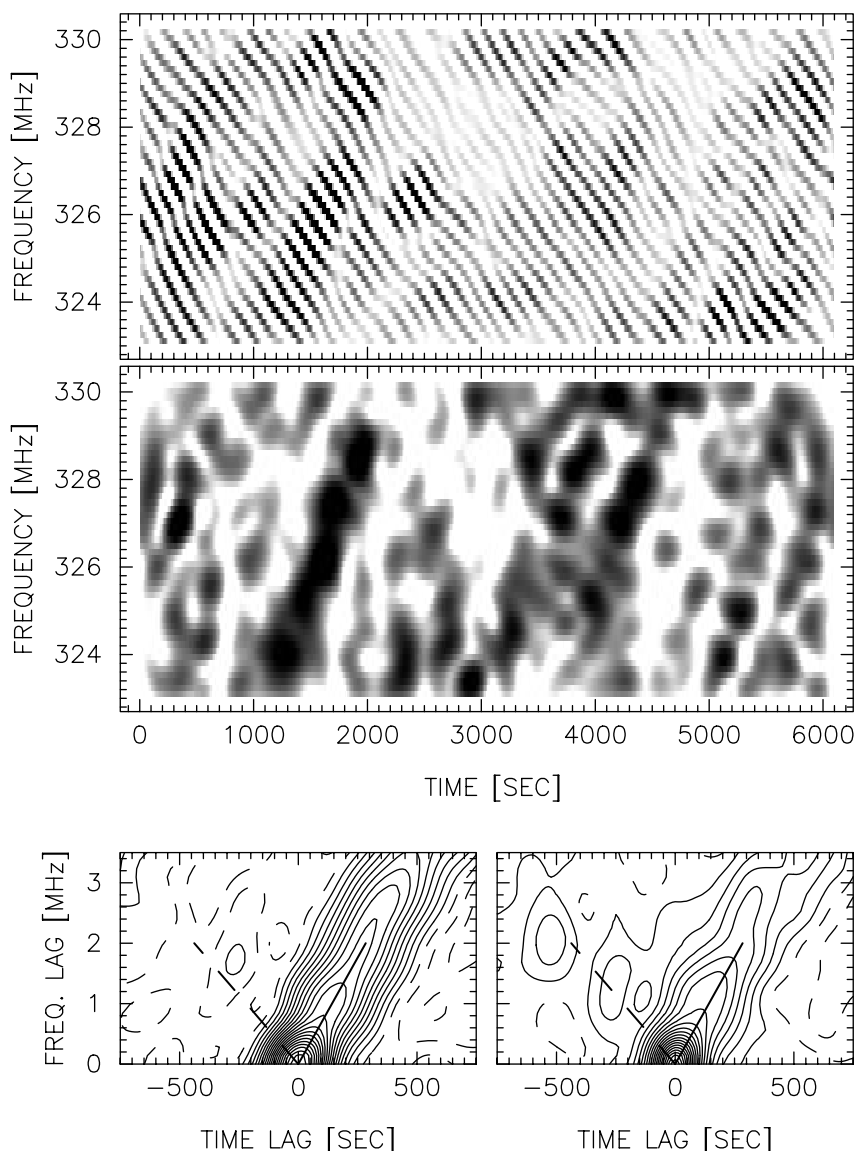

FIG. 2.—Dynamic spectrum for the second epoch (1994 April 30), after passing through the high pass filter (*top panel*) and the low pass filter (*middle panel*), as described in the text. The bottom panel shows the autocorrelation functions for the low pass filtered data, as described in the text. The solid and dashed lines represent the estimated drift slopes.
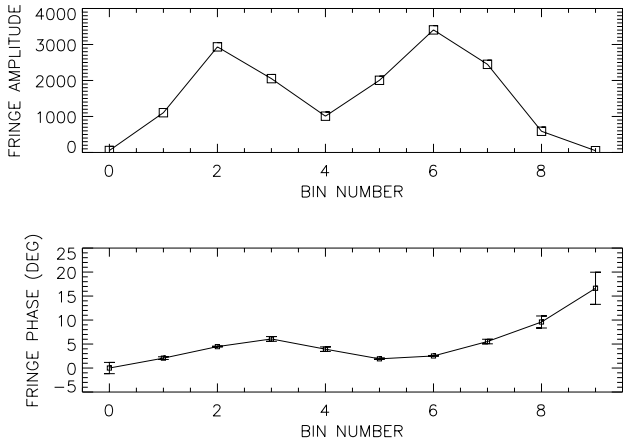
FIG. 3.—Variation of amplitude and phase of the periodic signal detected in the dynamic spectrum of the second epoch, as a function of longitude bin number.

tude of the diffractive scintles, and the phase shows discrete jumps at the scintle boundaries. Both of these effects reinforce the interstellar scintillation origin of the fringe pattern. These two effects are also responsible for the observed broadening of the spectral peak in the Fourier transform domain. The data were also put through a low pass filter that rejected the frequency corresponding to the periodic signal. The result is shown in the middle panel of Figure 2. Here the intensity gray scale is a logarithm scale that has been used to enhance the low-intensity features at the expense of the high-intensity features. It is clear from this figure that the dynamic spectra data show dual drift slopes, which is naturally expected when periodic fringe patterns are produced. The primary slope is the easily discernible positive slope (intensity scintles drifting along increasing frequency with increasing time). The secondary slope is a negative slope that is less prominent than the positive slope but can be seen in the form of V-shaped intensity structures as well as several individual scintles showing a negative slope. This is further exemplified by the autocorrelation function (ACF) plots shown in the bottom panel of Figure 2. The first of these is for the normal, low pass filtered data while the second is for the log-scaled, low pass filtered data. The ACF for the normal data is dominated by the primary drift slope, whereas the ACF for the log-scaled data clearly shows the presence of dual drift slopes. The solid and dashed lines on these plots mark the two estimated drift slopes whose values are found to be

$$\frac{dt}{df}\bigg|_1 = 142 \pm 25 \text{ s MHz}^{-1} ,$$

$$\frac{dt}{df}\bigg|_2 = -219 \pm 50 \text{ s MHz}^{-1} . \quad (2)$$

The error bars are 1 σ values, as estimated in Bhat et al. (1999b).

Our time resolution of 6 ms provided 10 time samples across the pulse width. Analysis showed the fringes to be present in each of these 10 phase-resolved dynamic spectra, with the average amplitude of the periodicity following the mean pulse shape of the pulsar (Fig. 3, *upper panel*). For the

dynamic spectra at each longitude bin, the bandpass filtering was done to obtain the periodic signal. The filtered data from one reference bin were then cross-correlated with similar data from each bin to obtain 10 temporal cross-correlation functions. In the computation of these cross-correlation functions, the maximum lags in time and frequency domains were restricted to 64 and 32, respectively, to reduce the effect of phase jumps in the dynamic spectra, such as those seen at scintle boundaries. Fourier transforms were taken for each of these cross-correlation functions, and the phase of the signal in the frequency bin corresponding to the periodicity in time was extracted to give the fringe phase versus longitude bin curve shown in the lower panel of Figure 3. The errors on these phase estimates were obtained by calculating the inverse tangent of the ratio of the rms noise in the off signal bins to the amplitude of the signal bin of the Fourier transform. The total variation of the phase of the fringes across the pulse ($\Delta\phi$) was found to be $\approx 15°$ (Fig. 3, *lower panel*). The phase variation was, however, not monotonic, showing two local extrema within the pulse which are located at bins 3 and 5. To check the robustness of our phase curve and the associated error bars, we repeated the above analysis for subsets obtained by splitting the data into two sections of 256 samples by 64 channels each. The phase curves obtained from these two subsets were found to match quite well with the result in Figure 3, except for the first and last longitude bins, where the deviations were somewhat larger, but still within the estimated error bars.

3. MODELING AND INTERPRETATION OF THE OBSERVATIONS

Our observations and data analysis indicate that the observed fringes are consistent with multiple imaging due to large-scale irregularities in the ISM. We model the observed refractive effects as being due to scattering from a discrete structure, such as a plasma lens, located at a distance L_S from the observer along the line of sight to the pulsar (Fig. 4a). Here the pulsar is located at P, at a distance L_P from the observer who is located at O. The scattering structure produces bending of radiation from the pulsar traveling along the directions P–S$_1$ and P–S$_2$ by angles β_{r1} and β_{r2}, respectively. The observer sees two dominant images of the pulsar, toward O–S$_1$ and O–S$_2$. The refracted wave fronts, with angles of arrival θ_{r1} and θ_{r2}, produce an interference pattern that results in periodic intensity modulations in the space and frequency domains at O. In addition, due to diffractive ISS, each of these two images is broadened to an angular spectrum of half-power width θ_d, the diffractive scattering width, which produces the diffractive intensity modulations at O. Because of relative motion between the observer and the scintillation pattern, quantified by the scintillation velocity (V_{ISS}), the spatial modulations of intensity are mapped to temporal modulations. The observation that the periodicities are much finer than the typical diffractive decorrelation widths in time and frequency requires $|\theta_{r1} - \theta_{r2}| > \theta_d$. This is equivalent to the presence of two scatter-broadened but well-separated images of the pulsar, as seen by the observer at O. The analytical treatment of such a scenario is very similar to the description given in Cordes & Wolszczan (1986), Cordes & Wolszczan (1988), and Rickett et al. (1997). However, since our final equations are somewhat different from the results in these papers, we go through the model in some detail.
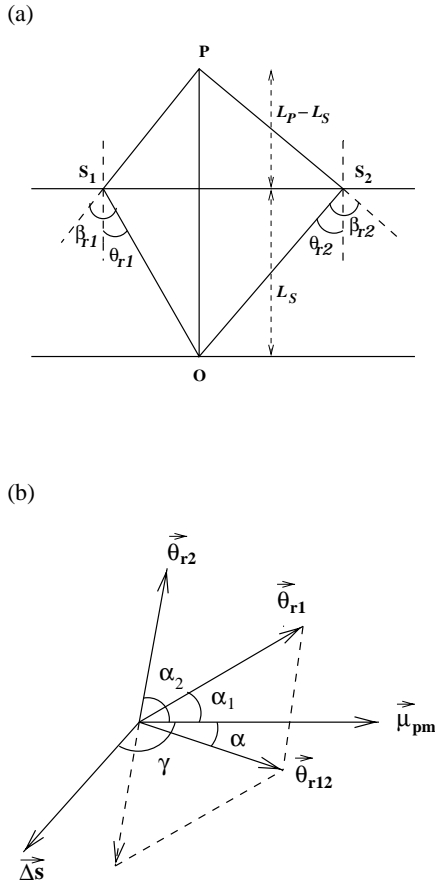
(a)

(b)

FIG. 4.—Schematics illustrating the geometry of the scattering event for (a) the plane containing the pulsar (P), the observer (O), and scattering structure, and (b) the plane transverse to the line of sight of the pulsar.

The electric field phasors at the observing plane, due to radiation from the two directions, can be written as

$$e_1(r, f) = a_1(r, f) \exp\left[i\Phi_1(r, f)\right],$$
$$e_2(r, f) = a_2(r, f) \exp\left[i\Phi_2(r, f)\right], \quad (3)$$

where a_1, a_2, Φ_1, and Φ_2 vary randomly with r and f due to diffractive scintillation, with typical correlation scales in space and frequency. The total intensity at the observing plane can then be written as

$$I(r, f) = a_1^2(r, f) + a_2^2(r, f)$$
$$+ 2a_1(r, f)a_2(r, f) \cos\left[\Phi_1(r, f) - \Phi_2(r, f)\right]. \quad (4)$$

Here the first two terms represent the diffractive scintillation patterns that would have been produced by each of the two images alone, and the third term produces the periodic intensity modulations, due to systematic variations of $\Phi_1 - \Phi_2$ as a function of r and f. The total phase change Φ_1 can be written as

$$\Phi_1(r, f) = \frac{k}{2}(\beta_{r1} - \theta_{r1})^2(L_P - L_S) + \frac{k}{2}\theta_{r1}^2 L_S$$
$$+ kr \cdot \theta_{r1} + \phi_{d1}. \quad (5)$$

The sum of the first two terms represents the geometric path delay due to the path P–S_1–O taken by the first wave front (with respect to the straight-line path P–O). The third term represents the wave-front delay at the observing plane due to the direction of arrival θ_{r1}. The last term represents the

random diffractive phase modulation. A similar expression holds for Φ_2. Using the relationship $\beta_{r1} = L_P \theta_{r1}/(L_P - L_S)$, the phase difference $\Phi_1 - \Phi_2$ can be expressed as

$$\Phi_1 - \Phi_2 = \frac{1}{2}\frac{kL_S L_P}{L_P - L_S}(\theta_{r1}^2 - \theta_{r2}^2) + kr \cdot (\theta_{r1} - \theta_{r2})$$
$$+ (\phi_{d1} - \phi_{d2}). \quad (6)$$

In order to obtain the expressions for the periodicities of the fringes in frequency and time, we express this phase difference as

$$\Phi_1 - \Phi_2 = 2\pi v_f df + 2\pi v_t dt + (\phi_{d1} - \phi_{d2}) + (\Phi_{1o} - \Phi_{2o}). \quad (7)$$

Here Φ_{1o} and Φ_{2o} are the values of Φ_1 and Φ_2 evaluated at the central frequency and time of observation. Comparing with equation (6), and mapping spatial variations to temporal variations using the scintillation pattern velocity (V_{ISS}), we have that v_t and v_f are given by

$$v_t = \frac{f_0}{c} V_{\mathrm{ISS}} \cdot (\theta_{r1} - \theta_{r2}), \quad (8)$$

$$v_f = \frac{3}{2c}\frac{L_S L_P}{L_P - L_S}(\theta_{r1}^2 - \theta_{r2}^2). \quad (9)$$

Using the relationship between scintillation velocity and proper-motion velocity for a thin screen case (e.g., eq. [5] of Gupta 1995), the expression for v_t can be rewritten as

$$v_t = \frac{f_0}{c}\frac{L_S L_P}{L_P - L_S}\mu_{\mathrm{pm}}(\theta_{r1}\cos\alpha_1 - \theta_{r2}\cos\alpha_2). \quad (10)$$

Here μ_{pm} is the amplitude of the pulsar's proper motion. The angles α_1, α_2 are the angles between μ_{pm} and θ_{r1}, θ_{r2}, as projected on the plane of the sky. These are illustrated in Figure 4b. Also shown there is the vector Δs representing the transverse separation between the emitting regions (in the pulsar's magnetosphere) corresponding to the leading and trailing edges of the pulsar profile and the angle γ that it makes with the proper-motion vector. The phase shift of the fringes between the leading and trailing edges of the profile can be expressed in terms of these quantities as

$$\Delta\phi = \frac{2\pi v_t \Delta s \cos(\gamma - \alpha)}{L_P \mu_{\mathrm{pm}} \cos\alpha}. \quad (11)$$

Here α is the angle between μ_{pm} and the resultant of θ_{r1} and θ_{r2}, as shown in Figure 4b. It is important to note that the above equation is independent of the exact location of the screen. This is because the lever-arm effect of Δs is exactly compensated for by the lever-arm effect of the pulsar's motion.

We note that our derivation of equations (6) and (9) ignores the contribution of the difference in the dispersive time delay along the two paths, as described by equation (6) of Rickett et al. (1997). This is because it is easily shown (as has been done by Rickett et al. 1997 for their data) that the contribution of this term to the total frequency-dependent delay is negligible. For example, if we assume that the observed value of v_f is entirely due to differential dispersive delay, it would require a fractional dispersion measure (DM) variation of 8.5×10^{-6} between the two paths. Using a typical value of 1×10^{-6} for fractional DM variations over 1 year timescales, reported for nearby pulsars by Phillips & Wolszczan (1991), we expect a fractional variation of

5.5×10^{-9} over the timescale of our event. Clearly, this is about 3 orders of magnitude smaller than required.

Assuming L_P, f_0, and μ_{pm} to be known quantities, there are six independent unknown quantities, θ_{r1}, θ_{r2}, Δs, α_1, α_2, and γ and only three independent equations, equations (9), (10), and (11). Thus, extra input is needed to invert the problem and obtain a solution for Δs. Some of this extra information is obtained from the slope of the drift bands produced by the two images contributing to the dynamic spectra, by using the relation between the drift slopes, the refractive angles and the proper motion. The two relevant equations are

$$\left.\frac{dt}{df}\right|_1 = -\frac{2\theta_{r1}\cos\alpha_1}{f_0\,\mu_{pm}}, \quad \left.\frac{dt}{df}\right|_2 = -\frac{2\theta_{r2}\cos\alpha_2}{f_0\,\mu_{pm}}. \quad (12)$$

It is interesting to note that equations (10) and (12) can be used to constrain the distances to the pulsar and the scattering structure. For this, using equation (12), we substitute for $\theta_{r1}\cos\alpha_1$ and $\theta_{r2}\cos\alpha_2$ in equation (10), to get

$$\frac{L_S L_P}{L_P - L_S} = 918 \pm 153 \text{ pc}, \quad (13)$$

for the known values of f_0, μ_{pm}, v_t, and the two drift slopes. The error bar on the above estimate takes into account the errors in the proper motion of the pulsar and the errors in the estimated drift slopes. Of these, the latter are the dominant source. A range of combinations of L_S and L_P values can be found that satisfy this relationship. For example, if the scattering structure is assumed to be located midway to the pulsar ($L_S = L_P/2$), then the distance to the pulsar needs to be 3.4 times the current estimate of 270 pc. This is rather unlikely. On the other hand, if the current distance estimate is taken to be correct, it requires the scattering structure to be located at $L_S = (0.77 \pm 0.2)L_P$. The error in this estimate is dominated by the error in the distance estimate (taken to be 20%) for this pulsar. We note that this estimate of the distance to the scatterer is strikingly close to the distance to the boundary of the Local Bubble in this direction, as inferred by Bhat, Gupta, & Rao (1998) from their detailed study of pulsar scintillation in the local ISM. Their model predicts that the cavity of the Local Bubble is surrounded by an ellipsoidal shell of enhanced scattering material. Along the line of sight to this pulsar, this shell is estimated to contribute about 70% of the total scattering. From their model, the distance to the shell in this direction is expected to be in the range 212–217 pc ($0.79L_P$ to $0.80L_P$). Thus, it is very likely that the scattering structure responsible for this fringing event is located in the shell of the Local Bubble.

Using equations (9), (11), and (12) and the measurement of the phase shift of the fringes between the leading and trailing edges of the profile, constraints can be placed on the minimum value of Δs in the following manner. For a given choice of one of the unknowns (say, θ_{r1}), unique values can be calculated for α_1, θ_{r2}, and α_2 (and hence α and θ_{r12}). Then, assuming the extreme case of $\gamma = \alpha$, a lower limit to Δs for the given choice of θ_{r1} can be calculated as

$$\Delta s_{\min} = \frac{\Delta\phi L_P\,\mu_{pm}\,\cos\alpha}{2\pi v_t}. \quad (14)$$

This procedure has been followed for a plausible range of values for θ_{r1} given by $|\theta_{r1}| < 20\theta_d$. A value of $\Delta\phi = 15°$ has been used in these calculations. The results are sum-
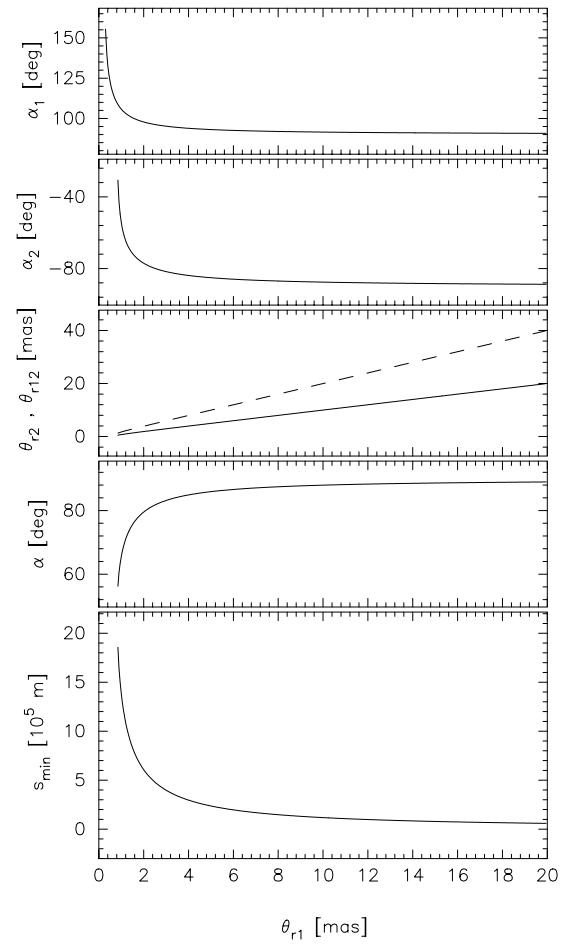

FIG. 5.—Variation of the different quantities as a function of refractive scattering angle, θ_{r1}. In the middle panel the solid line is for θ_{r2} and the dashed line is for θ_{r12}.

marized in Figure 5, where various relevant quantities are plotted against θ_{r1}. From these, it can be seen that the inferred value of $\Delta s_{\min}$ ranges from $\approx 1 \times 10^6$ m to $\approx 1 \times 10^5$ m for θ_{r1} ranging from ≈ 1 to ≈ 15 mas. The inferred value of θ_{r2} follows θ_{r1} closely, and the angles α_1, α_2 systematically increase in amplitude toward 90° (but with opposite signs) with increasing θ_{r1}. Consequently, the resultant angle α increases from $\approx 55°$ to $\approx 90°$ with increasing θ_{r1}. This means that the smaller values of $\Delta s_{\min}$ are obtained when the orientation of the scattering structure is close to being orthogonal to the direction of proper motion of the pulsar.

4. DISCUSSION

Our observations and analysis of the phase shift of the fringes across the pulse window clearly reveal that the pulsar magnetosphere has been resolved during these observations. There are two significant aspects of the variation of the fringe phase shown in Figure 3. The first is the inferred separation between the emission regions corresponding to the leading and trailing edges of the pulsar profile, when they are radiating toward the observer (i.e., the total size of the emission region). The second is the implications of the nonmonotonic variation of the fringe phase as a function of pulse longitude.

Addressing the first aspect, we first note that the diffractive scattering angle (θ_d) for this epoch is estimated to be

≈ 0.72 mas. The standard Kolmogorov model for the spectrum of electron density fluctuations in the ISM predicts that the rms value of the refractive scattering angle should be $\lesssim \theta_d$ (e.g., Rickett 1990). Assuming that individual realizations of the refractive angles could be $\approx 3-5$ times larger than the rms values, θ_{r1} and θ_{r2} values of $\approx 2-4$ mas are feasible. From Figure 5, this gives the likely value for Δs_{min} to be $\approx 3 \times 10^5$ m. Smaller values of Δs_{min} require appreciably larger values of θ_{r1} and θ_{r2} and are much less likely for the simple Kolmogorov model. Of course, if the spectrum is steeper than Kolmogorov or has a low-frequency enhancement corresponding to refractive scales, larger values of θ_{r1} and θ_{r2} would be feasible. Evidence for such enhanced refraction has been reported for several different lines of sight (e.g., Rickett et al. 1997; Fiedler et al. 1994). In particular, for this line of sight, Bhat, Gupta, & Rao (1999a) find that the slope of the spectrum, estimated from diffractive and refractive scintillation measurements, is in excess of 11/3, being close to 3.78. In any case, Figure 5 indicates that Δs_{min} appears to reach an asymptotic value of $\approx 8 \times 10^4$ m for large values of θ_{r1}. Thus it is unlikely that a value of $\Delta s_{min} = 3 \times 10^5$ m would be more than a factor of 2 larger than the smallest value that more complicated versions of the Kolmogorov model would allow.

From this estimate of Δs, the altitude at which the observed radiation is emitted in the pulsar magnetosphere can be calculated. This requires two assumptions to be made: the first is that the pulsar's magnetic field has a simple dipole geometry, and the second is that the radiation corresponding to the leading and trailing edges of the profile is emitted at the same height and is beamed tangential to field lines located symmetrically about the magnetic axis. This geometry is illustrated in Figure 5 of Cordes, Weisberg, & Boriakoff (1983). Under these conditions, it can be shown that the emission altitude is given by $r_{em} \approx 3\Delta s/\Delta\theta$, where $\Delta\theta$ is the observed pulse width between the leading and trailing edges of the profile, expressed in radians. The derivation of this result requires the small-angle approximation to be valid for the angle between the tangent to the field line and the magnetic axis of the pulsar. Using $\Delta s = \Delta s_{min}$ gives a lower limit on r_{em} of 2.6×10^6 m. This is 4.5% of the value of the light-cylinder radius for this pulsar.

Our inferred values of $\Delta s_{min} \approx 3 \times 10^5$ m and $r_{em} \approx 3 \times 10^6$ m are the smallest lower limits of all currently available estimates using the technique of multiple imaging (Kuz'min 1992; Wolszczan & Cordes 1987; Wolszczan et al. 1988). Furthermore, it is the only value that is also consistent with the upper limit of $\Delta s < 1 \times 10^6$ m obtained for this pulsar from diffractive scintillation techniques (Cordes et al. 1983). We also note that our values are very similar to those obtained for this pulsar by Smirnova & Shishov (1989), from an analysis of interstellar scintillations at 102 MHz. Further, our estimates are very similar to the size of the emission region for the Vela pulsar (≈ 500 km) obtained by Gwinn et al. (1997) from VLBI observations of the scintillation pattern. Thus there appears to be some amount of recent evidence from scintillation studies that transverse extents of pulsar emission regions may be $\sim 10^5$ m.

Although our inferred values for emission altitude are among the smallest reported values obtained from the scintillation technique, they are still somewhat larger than those obtained from other techniques for estimating emission altitudes. For example, period–pulse-width relation studies (e.g., Rankin 1990; Gil 1991) suggest emission altitudes to be $\approx 1 \times 10^5$ to 1×10^6 m. A similar range is estimated from the technique of Blaskiewicz, Cordes, & Wasserman (1991), where measurement of the time lag between the total intensity and polarization position angle profiles is used to estimate the emission altitude. Emission altitudes estimated from the measurement of times of arrival for different frequencies, using pulsar timing measurements, are shown to have an upper limit of 3% of the light-cylinder radius (Cordes 1992; Phillips 1992). More recently, Kijak & Gil (1998) and Kijak & Gil (1997) have done a thorough study of the estimation of the emission altitudes for several pulsars using a refined version of the period–pulse-width relationship. They have estimated the emission altitudes for 16 long-period pulsars and 6 millisecond pulsars at different frequencies ranging from a few hundred MHz to 10 GHz. From the results for PSR B1133+16 given in Figure 2 of Kijak & Gil (1998), the emission altitude at 327 MHz can be estimated as 7.5×10^5 m, which is only about 3 times smaller than our estimate. Thus, the new results presented here have somewhat reduced the discrepancy that prevails between the results from the scintillation technique and the other methods of estimating pulsar emission altitudes.

The observed nonmonotonic variation of the fringe phase as a function of pulse longitude implies, to first order, that the inferred transverse separations of the emission regions do not increase monotonically across the pulsar profile. Similar nonmonotonic variations of fringe phase have been observed for this pulsar (Wolszczan et al. 1988) and for PSR B1237+25 (Wolszczan & Cordes 1987). In the work of Smirnova & Shishov (1989) and Smirnova, Shishov, & Malofeev (1996), the inferred transverse separations as a function of pulse longitude also show a nonmonotonic variation for several pulsars (including PSR B1133+16). Thus such behavior does not appear to be an uncommon feature.

There are two models that can explain such results. The first is the case where the magnetic field in the emission regions is not strictly dipolar. The other possibility is that the emission altitudes at a given frequency are not constant across the polar cap. The shape of the polarization angle curve can be used to discriminate between these two possibilities. If the polarization angle curve follows the "S-shape" curve as described by the Radhakrishnan & Cooke (RC) model for a dipole geometry (Radhakrishnan & Cooke 1969), then the first model can be ruled out. For PSR B1133+16, the observed polarization angle curve does not appear to follow such a model. In fact, the shape of the polarization curve is strikingly similar to the fringe phase curve. This can be seen by comparing the fringe phase curve in Figure 3 with the polarization angle curve at the nearby frequency of 408 MHz (e.g., Fig. B.24 of Gould 1994). Similarly, the fringe phase curve obtained for this pulsar by Wolszczan et al. (1988) for the fringing episode at a frequency of 1400 MHz, though very different from our curve in Figure 3, is very similar to the position angle curve at 1400 MHz (e.g., Fig. 16 of Stinebring et al. 1984 and Fig. B.24 of Gould 1994). We note in particular that the longitudes at which the position angle deviates by large amounts from a smooth, monotonic curve are also the longitudes where the fringe angle curve shows significant deviations. It is very unlikely that such a similarity between the fringe angle curves at two different frequencies and their respective position angle curves is coincidental.

Although the deviation from the RC model curve for this pulsar may, at first sight, indicate that the field is not dipolar, it is now well understood that the observed deviation is due to the phenomenon of orthogonal polarization modes (e.g., Stinebring et al. 1984). In this picture, the position angle at any longitude can take on one of two values at any instant—the normal position angle value and a value 90° different from this. The longitudes at which the secondary, orthogonal mode occurs more frequently will show a mean polarization angle that is about 90° different from the overall position angle curve produced by the primary mode. Such an effect is clearly seen in part of the first component of the profile for this pulsar, in the 1400 MHz data (Stinebring et al. 1984). For longitudes where the dominance of the primary mode over the secondary mode is not well established, the deviations of position angle are not as dramatic. This could give rise to the smoother (but still deviating from the RC model) polarization angle curve seen at 400 MHz for this pulsar. On plotting the mode-separated position angle curves, each is found to follow the RC model, while maintaining a separation of 90°. It is not clear whether orthogonal polarization states are intrinsic to the pulsar emission mechanism or are an artifact of propagation through the magnetospheric plasma.

Since the fringe angle curve shows significant deviations from a monotonic curve at the same longitudes at which the secondary polarization mode is dominant, it suggests that the emission regions for the secondary mode are significantly offset in location from the monotonically increasing separation of the emission regions representing the primary mode. However, since both modes at a given longitude are expected to originate at the same field line, this offset in separation is unlikely to be along the polar cap (at a constant altitude). Rather, this offset is more likely produced by a difference in emission altitudes for the two modes, while following the same field line. This suggests that the orthogonal polarization modes are likely to be a propagation effect rather than an intrinsic property of the emission mechanism.

Our results and inferences are in agreement with models where refraction in the pulsar magnetosphere is used to explain the phenomenon of orthogonal polarization modes. For example, Barnard & Arons (1986) have shown that the relativistically outflowing plasma in the open field line region of the pulsar magnetosphere can act as a "polarizing beam splitter." In their model, X-mode and O-mode waves, having intrinsically orthogonal polarization states, are produced that get separated by large angles because the X-mode wave travels in a straight line from the point of emission, while the O-mode wave is ducted along the magnetic field line, to a point higher in the magnetosphere from which it escapes, and follows a straight-line trajectory. Gallant (1996) has shown how a combination of such X-mode waves and ducted O-mode waves can produce the nonmonotonic variation of the lateral displacement of the emission regions across the pulse profile, as inferred in the scintillation studies. Such a model would naturally predict a similarity between the phase angle curves of the fringing events and the polarization angle curve.

Further data of multiple imaging events (preferably multiple epochs for a pulsar) with careful measurements of drift slopes in the dynamic spectra should provide better constraints on the pulsar emission geometry. Such observations might also help to infer properties of the magnetosphere, such as the plasma density, and help in studying propagation effects in pulsar magnetospheres.

5. CONCLUSIONS

We have reported the observations and analysis of a multiple imaging event for PSR B1133+16 at a frequency of 327 MHz. The dynamic spectra show clear periodic intensity modulations as a function of time and frequency. In addition, dual drift slopes are clearly seen in the dynamic spectra. The fringes are seen in each of the 10 bins across the pulse profile. The phase of the fringes shows a change of $\approx 15°$ between the leading and trailing edges of the pulsar profile, implying that the pulsar magnetosphere has been resolved during these observations. However, the observed fringe phase variation with pulse longitude is non-monotonic. We have modeled the observed fringes as being produced by multipath propagation due to refraction from a discrete scattering object in the ISM. Expressions have been derived for the dual drift slopes, the fringe periodicities in time and frequency, and the transverse separation of emission regions as a function of the measured fringe phase shift. From the measurements of the fringe period in time and the values of the dual drift slopes, we conclude that the refracting structure is located at a distance that matches very well with the expected location, in this direction, of the enhanced scattering shell of the Local Bubble. Thus it is very likely that the enhanced scattering required to produce this multiple imaging is provided by the shell of the Local Bubble. Using our model, we are able to constrain the minimum size of the emission region, Δs_{min}, to be $\approx 3 \times 10^5$ m. For a dipole geometry, this implies an emission altitude in the magnetosphere of $\approx 2.6 \times 10^6$ m, which is 4.5% of the light-cylinder radius for this pulsar. These estimates of Δs_{min} and emission altitude provide the smallest lower limits of all currently available estimates using the technique of multiple imaging. The estimated emission altitude is, however, larger than that obtained using other techniques such as multi-frequency timing, polarization, and period–pulse-width relation studies. Refraction in the pulsar magnetosphere is the likely explanation for this disagreement. The non-monotonic variation of the fringe phase with pulse longitude for this pulsar matches very closely the variation of the polarization angle curve with pulse longitude. This is found to be true at two different radio frequencies. This is interpreted as implying that the orthogonal polarization modes for this pulsar are emitted at different altitudes in the pulsar magnetosphere. Such a picture is in agreement with models where refraction plays an important role in the pulsar magnetosphere.

REFERENCES

Barnard, J. J., & Arons, J. 1986, ApJ, 302, 138
Bhat, N. D. R., Gupta, Y., & Rao, A. P. 1998, ApJ, 500, 262
———. 1999a, ApJ, in press
Bhat, N. D. R., Rao, A. P., & Gupta, Y. 1999b, ApJ, in press
Blaskiewicz, M., Cordes, J. M., & Wasserman, I. 1991, ApJ, 370, 643

Cordes, J. M. 1992, in IAU Colloq. 128, The Magnetospheric Structure and Emission Mechanisms of Radio Pulsars, ed. T. H. Hankins, J. M. Rankin, & J. A. Gil (Zielona Gora: Pedagogical Univ. Press), 253
Cordes, J. M., Weisberg, J., & Boriakoff, V. 1983, ApJ, 268, 370
Cordes, J. M., & Wolszczan, A. 1986, ApJ, 307, L27

Cordes, J. M., & Wolszczan, A. 1988, in AIP Conf. Proc. 174, Radiowave Scattering in the Interstellar Medium, ed. J. M. Cordes, B. J. Rickett, & D. C. Backer (New York: AIP), 212

Fiedler, R., Dennison, B., Johnston, K. J., Waltman, E. B., & Simon, R. S. 1994, ApJ, 430, 581

Gallant, Y. A. 1996, in IAU Colloq. 160, Pulsars: Problems and Progress, ed. S. Johnston, M. A. Walker, & M. Bailes (San Francisco: ASP), 431

Gil, J. A. 1991, A&A, 243, 219

Gould, D. M. 1994, Ph.D. thesis, Univ. Manchester

Gupta, Y. 1995, ApJ, 451, 717

Gupta, Y., Rickett, B. J., & Lyne, A. G. 1994, MNRAS, 269, 1035

Gwinn, C. R., et al. 1997, ApJ, 483, L53

Hewish, A. 1980, MNRAS, 192, 799

Kijak, J., & Gil, J. 1997, MNRAS, 288, 631

———. 1998, MNRAS, 299, 855

Kuz'min, O. A. 1992, in IAU Colloq. 128, The Magnetospheric Structure and Emission Mechanisms of Radio Pulsars, ed. T. H. Hankins, J. M. Rankin, & J. A. Gil (Zielona Gora: Pedagogical Univ. Press), 287

Phillips, J. A. 1992, ApJ, 385, 282

Phillips, J. A., & Wolszczan, A. 1991, ApJ, 382, L27

Radhakrishnan, V., & Cooke, D. J. 1969, Astrophys. Lett., 3, 225

Rankin, J. M. 1990, ApJ, 352, 247

Rickett, B. J. 1990, ARA&A, 28, 561

———. 1996, in IAU Colloq. 160, Pulsars: Problems and Progress, ed. S. Johnston, M. A. Walker, & M. Bailes (San Francisco: ASP), 439

Rickett, B. J., Lyne, A. G., & Gupta, Y. 1997, MNRAS, 287, 739

Smirnova, T. V., & Shishov, V. I. 1989, Pis'ma AZh, 15, 443; English transl. Soviet Astron., 15, 191

Smirnova, T. V., Shishov, V. I., & Malofeev, V. M. 1996, ApJ, 462, 289

Stinebring, D. R., Cordes, J. M., Rankin, J. M., Weisberg, J. M., & Boriakoff, V. 1984, ApJS, 55, 247

Wolszczan, A., Bartlett, J. E., & Cordes, J. M. 1988, in AIP Conf. Proc. 174, Radiowave Scattering in the Interstellar Medium, ed. J. M. Cordes, B. J. Rickett, & D. C. Backer (New York: AIP), 145

Wolszczan, A., & Cordes, J. M. 1987, ApJ, 320, L35